The Journal of the Astronautical Sciences (2026) 73:21
https://doi.org/10.1007/s40295-025-00556-w

RESEARCH

Orbiting Spacecraft Relative Motion in the Inertial Frame

Julian Hammerl[1] · **Hanspeter Schaub**[1]

Received: 16 July 2025 / Accepted: 10 November 2025

Abstract

While the description of orbiting spacecraft relative motion is usually done in the rotating Hill frame due to analytical first-order solutions and the intuitive shape of the relative orbits, it is disadvantageous for mission design requirements that are fixed in the inertial frame. This includes distributed space telescopes aligned with inertial targets as well as formations and servicing operations with inertially fixed keep-in/out zones, e.g. constraints imposed by the Sun direction. This paper studies the analytical first-order inertial frame solutions of the relative motion of orbiting spacecraft and derives geometrically meaningful relative orbit elements and invariants of motion for inertial frame relative orbits. It is found that the relative motion for a circular chief orbit corresponds to the motion of an epitrochoid. For elliptic chief orbits, the inertial frame relative orbits are stretched and distorted compared to the epitrochoid curve for circular chief orbits, but similar relative orbit elements are defined as well. Finally, the variational equations of the inertial relative orbit elements are developed and their use is demonstrated through an asymptotically stabilizing continuous feedback control law.

Keywords Relative motion · Inertial frame · Orbit elements · Natural motion

✉ Julian Hammerl
julian.hammerl@colorado.edu

Hanspeter Schaub
hanspeter.schaub@colorado.edu

[1] Department of Aerospace Engineering Sciences, University of Colorado Boulder, 3775 Discovery Drive, Boulder, CO 80303, USA

Published online: 26 February 2026

1 Introduction

The relative motion of an orbiting deputy spacecraft with respect to a chief spacecraft is most commonly described in a rotating frame aligned with the radial position vector of the chief, often referred to as the Hill frame [1] or the Local-Vertical-Local-Horizontal (LVLH) frame. Some of the benefits of the description in the Hill frame are the existence of simple analytical solutions for circular orbits, such as for the Clohessy–Wiltshire equations [2], the resulting intuitive shape of the relative orbits, and the fact that the out-of-plane motion is uncoupled from the in-plane motion. For bounded motion (no drift motion), the relative orbit has the shape of an ellipse (or in simpler cases a single point) in the orbital plane and is either centered at the chief or offset in the along-track direction. A difference in the semi-major axis of the two spacecraft results in drift motion in the along-track direction. In the most complex case for drift motion, the relative orbit is a spiral motion about the along-track direction.

However, the description in the Hill frame is disadvantageous for some mission design requirements. Distributed space telescopes have been proposed for large-aperture telescope architectures that cannot be realized with a single spacecraft [3, 4]. Instead of having one spacecraft with all telescope components, a two-spacecraft formation consisting of one spacecraft equipped with the lens and another spacecraft equipped with the sensor is used. The VIrtual Super Optics Reconfigurable Swarm (VISORS) mission is a demonstration for such a concept [5]. Because a space telescope is commonly aligned with inertial targets, the description of relative motion is beneficial in the inertial frame, despite inertial frame relative orbits being more complex. Missions such as New World Observer [6], where a giant starshade [7] is used to block the light from a star while searching for exoplanets, may also benefit from a description in the inertial frame. Other missions such as the Terrestrial Planet Finder [8] (TPF, canceled in 2011) and Large Interferometer For Exoplanets [9] (LIFE, in development) proposed to use a nulling interferometer consisting of multiple spacecraft to search for exoplanets. Such exoplanet search missions are planned to be located around the Sun-Earth L2 Lagrange point. Thus, the relative motion occurs within the regime of the three body problem and requires different dynamics models [10–13], in contrast to the relative motion of two spacecraft orbiting one planet as explored in this current work. Other mission concepts call for formations where the spacecraft never eclipse each other, or where one spacecraft is desired to be in the shadow of the other for prolonged periods. For example, the Project for On-Board Autonomy 3 (PROBA-3) mission is a formation flying demonstration mission that launched in December 2024, consisting of an occulter spacecraft that casts the Sun's shadow on a coronagraph spacecraft to study the Sun's faint corona [14]. For spacecraft orbiting Earth, this imposes a keep-out or keep-in zone that is fixed in a quasi-inertial frame (because the Sun direction changes slowly). Several of these proposed missions are illustrated in Fig. 1.

In a similar fashion, such inertially fixed keep-out or keep-in zones may be introduced for spacecraft servicing and docking operations. For example, during rendezvous it may be beneficial to maintain certain lighting conditions, or to keep line-of-sight with another inertially fixed target. Relative motion constraints for

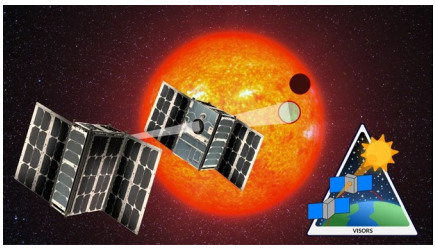

(a) VISORS [1]

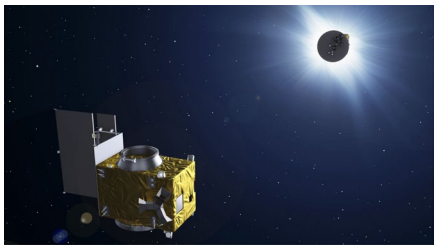

(b) Proba-3 [2]

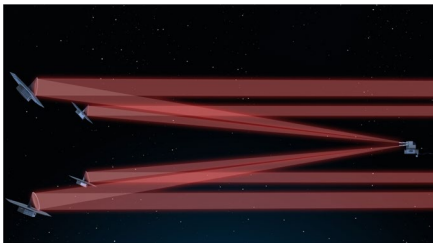

(c) LIFE mission [3]

Fig. 1 Concept figures of space missions with inertial constraints.[1]https://slab.stanford.edu/projects/visors. (Consulted on: 06/27/2025) [2]https://www.esa.int/Enabling_Support/Space_Engineering_Technology/Proba_Missions/About_Proba-3. (Consulted on: 06/27/2025) [3]https://ethz.ch/en/news-and-events/eth-news/news/2023/04/a-key-experiment-for-the-life-space-mission.html. (Consulted on: 06/27/2025)

docking operations are often described in the body frame of the target spacecraft. If the target satellite is not rotating, the body frame of the target remains aligned with the inertial frame, and the insights from the inertial frame relative motion can be applied to the body frame. Finally, plasma wakes also motivate a relative motion description in the inertial frame. Plasma wakes form in the anti-ram-side direction behind the spacecraft if the ion thermal velocity is greater than the electron thermal velocity [15], where the ram-side is determined by the spacecraft velocity relative to the bulk velocity of the ions. The plasma and spacecraft charging dynamics are more complex inside this wake, and inter-spacecraft electrostatic forces may also be stronger [16]. This motivates to stay inside the wake to study the plasma and spacecraft charging dynamics, or outside to minimize electrostatic perturbations [17]. In Low Earth Orbit (LEO), the ion bulk velocity is negligibly small, so the wake is approximately fixed in the spacecraft velocity frame [18] (or Hill frame for a circular orbit). Outside Earth's magnetosphere, in contrast, the ions move with the solar wind. If the spacecraft velocity is negligibly small compared to the solar wind velocity, the wake forms in the anti-sun direction and is quasi-inertially fixed [19]. Such cislunar plasma wakes extend several spacecraft widths behind the leading spacecraft, resulting in wake lengths in the order of 10 s of meters [20]. Hill frame fixed vs. Inertial frame fixed constraints are illustrated in Fig. 2.

The aforementioned mission scenarios benefit from a relative motion description of the orbiting satellites in the inertial frame. A large body of work exists in the literature about relative motion described in the Hill frame, as extensively reviewed in

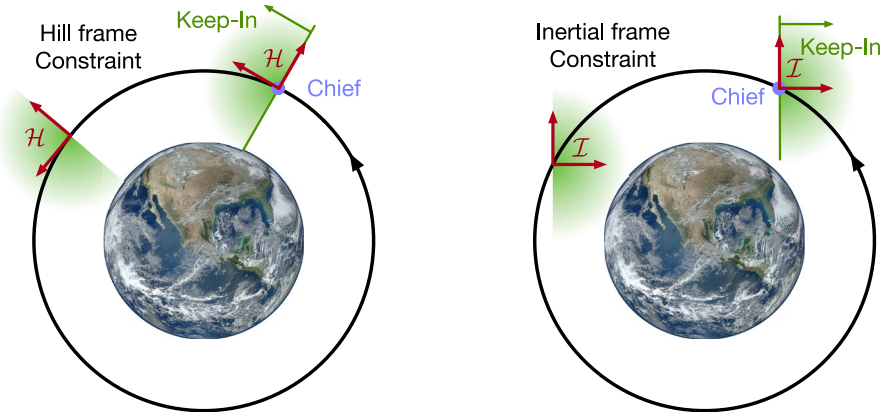

Fig. 2 Illustration of Hill frame vs. Inertial frame constraints

Ref. [21]. The various models may be categorized by the reference orbit, such as near-circular [22, Chapter 4] or eccentric orbit [23]; by the solution form, such as linear [2, 24] or nonlinear [25]; and by the perturbations considered in the dynamics, such as earth oblateness (J_2), atmospheric drag, thrust maneuvers, solar radiation pressure or third body effects by the Sun or Moon. Additionally, instead of using the cartesian relative position and velocity in the Hill frame as the state, some models use states that are based on relative orbit elements (ROEs), such as the Hill-Clohessy-Wiltshire (HCW) invariants [2, 26], mean orbit element differences (MOED) [27–32] or relative eccentricity and inclination vector (E/I-vector) [33, 34]. While mappings exist to map between the various state representations [21], they usually map the ROEs back to the cartesian state in the Hill frame. Some work exists for relative motion in the spacecraft velocity frame [35], which is especially advantageous for atmospheric entry trajectories of two spacecraft or highly eccentric chief orbits. Relative motion descriptions based on the relative state in the inertial frame have not been explored.

Constraints such as keep-in and keep-out zones are also usually described in the Hill frame or body frame of the target. Hill frame fixed keep-out zones are convenient for situations with larger spacecraft separation distances such as safety ellipses during approach of a spacecraft to the International Space Station [36]. Body frame fixed keep-out zones are often used for docking operations [37]. Inertially constrained relative motion around a planet has only been studied for a very specific orbit to maximize the average power generation [38, 39], but keep-out zones or general orbits were not investigated. For the problem at hand, inertially fixed constraints could be treated as time-varying constraints in the Hill frame. However, the many aforementioned motivations of describing the relative motion of two spacecraft in the inertial frame call for a more general approach to this problem to better understand the relative motion in the inertial frame.

This paper develops an elegant analytical description of the relative motion of two spacecraft in the inertial frame, where new geometrically meaningful relative motion invariants are introduced. A background about relevant coordinate frames and relative motion descriptions in the Hill frame is provided in Sect. 2. The solution of the

relative motion in the inertial frame and the inertial frame relative orbit elements are derived and discussed for circular chief orbits in Sect. 3 and for elliptic chief orbits in Sect. 4. A control law based on this new set of relative orbit elements is derived and implemented in Sect. 5. Finally, the inertial relative orbit design is applied to an on-orbit servicing example with plasma wakes in Sect. 6.

2 Relative Motion Problem Statement

Two spacecraft are orbiting a central body in close proximity to each other. Given the inertial position of the chief (target spacecraft) $\boldsymbol{r}_c$ and the deputy (servicing spacecraft) $\boldsymbol{r}_d$, the relative position vector is defined as

$$\boldsymbol{\rho} = \boldsymbol{r}_d - \boldsymbol{r}_c \tag{1}$$

and used to describe the relative motion of the two spacecraft.

This section reviews a set of frames and relative orbit descriptions that form the building blocks for the new developments of this paper. First, the relevant frames and coordinate transformations are defined to allow for a transition from the Hill frame to the Inertial frame. Then, two classical Hill frame relative motion descriptions are reviewed that are subsequently transformed to the Inertial frame in Sects. 3 and 4.

2.1 Relevant Coordinate Frames

The relative motion is commonly described in a rotating frame $\mathcal{H} : \{\hat{\boldsymbol{h}}_r, \hat{\boldsymbol{h}}_\theta, \hat{\boldsymbol{h}}_h\}$ centered at the chief C with axes

$$\hat{\boldsymbol{h}}_r = \frac{\boldsymbol{r}_c}{|\boldsymbol{r}_c|} \tag{2}$$

$$\hat{\boldsymbol{h}}_\theta = \hat{\boldsymbol{h}}_h \times \hat{\boldsymbol{h}}_r \tag{3}$$

$$\hat{\boldsymbol{h}}_h = \frac{\boldsymbol{r}_c \times \dot{\boldsymbol{r}}_c}{|\boldsymbol{r}_c \times \dot{\boldsymbol{r}}_c|} \tag{4}$$

where $\dot{\boldsymbol{r}}_c$ is the inertial velocity of the chief. This frame is referred to as the Hill frame [1] and is similar to the Local-Vertical-Local-Horizon (LVLH) frame $\mathcal{L} : \{\hat{\boldsymbol{l}}_1 = \hat{\boldsymbol{h}}_\theta,\ \hat{\boldsymbol{l}}_2 = -\hat{\boldsymbol{h}}_h,\ \hat{\boldsymbol{l}}_3 = -\hat{\boldsymbol{h}}_r\}$. The first axis of the Hill frame is aligned with the orbit radial direction of the chief, the third axis is aligned with the orbit normal direction, and the second axis completes the right-handed coordinate frame. Another frame $\mathcal{N} : \{\hat{\boldsymbol{n}}_1, \hat{\boldsymbol{n}}_2, \hat{\boldsymbol{n}}_3\}$ is used with inertially fixed directions of the frame axes $\hat{\boldsymbol{n}}_1, \hat{\boldsymbol{n}}_2, \hat{\boldsymbol{n}}_3$. Figure 3 illustrates the Hill frame and Inertial frame.

The direction cosine matrix (DCM) [HN] to map from the inertial frame $\mathcal{N}$ to the Hill frame $\mathcal{H}$ may be obtained using the chief orbit elements. Using the DCMs for a generic rotation θ about the first frame axis

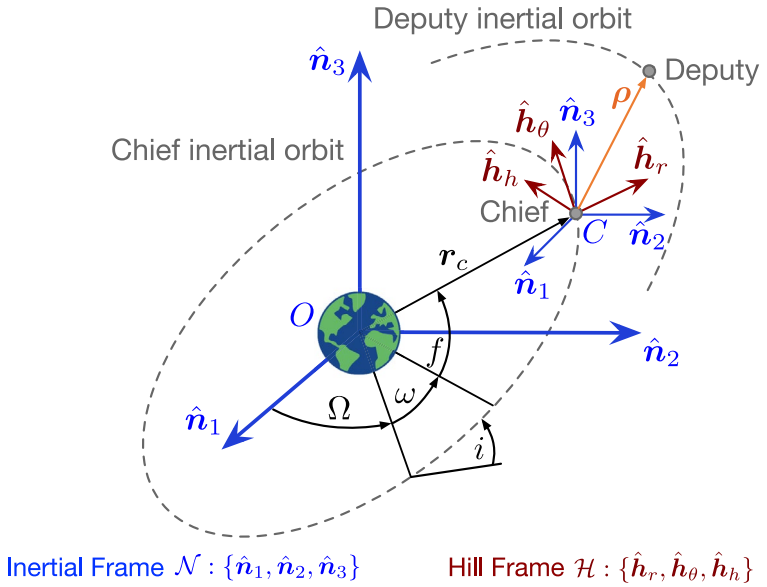

Fig. 3 Illustration of Hill frame and Inertial frame: The Hill frame $\mathcal{H}$ is centered at the chief and rotates as the chief orbits the central body, with $\hat{\boldsymbol{h}}_r$ aligned with the orbit radial direction of the chief and $\hat{\boldsymbol{h}}_h$ aligned with the orbit normal direction. The inertial frame $\mathcal{N}_O$ is located at the central body with fixed directions of the frame axes. A moving frame $\mathcal{N}_C$ is used that is centered at the chief, but its axes remain aligned with the inertial frame

$$[M_1(\theta)] = \begin{bmatrix} 1 & 0 & 0 \\ 0 & \cos\theta & \sin\theta \\ 0 & -\sin\theta & \cos\theta \end{bmatrix} \tag{5}$$

and the generic DCM about the third frame axis

$$[M_3(\theta)] = \begin{bmatrix} \cos\theta & \sin\theta & 0 \\ -\sin\theta & \cos\theta & 0 \\ 0 & 0 & 1 \end{bmatrix} \tag{6}$$

the DCM for a (3-1-3) Euler angle rotation (Ω, i, ω) is written as [40]

$$[PN(\Omega, i, \omega)] = [M_3(\omega)][M_1(i)][M_3(\Omega)] \tag{7}$$

where Ω is the right ascension of the ascending node (RAAN), i is the orbit inclination, and ω is the argument of periapsis. The frame $\mathcal{P} : \{\hat{\boldsymbol{p}}_1, \hat{\boldsymbol{p}}_2, \hat{\boldsymbol{p}}_3\}$ is the perifocal frame, in which the first axis points from the focus of the orbit (the central body) to periapsis, the third axis points in the chief orbit angular momentum direction, and the second axis completes the right-handed coordinate frame. To map from the perifocal frame $\mathcal{P}$ to the Hill frame $\mathcal{H}$, another rotation around the third frame axis is performed using the true anomaly f

$$[HP(f)] = [M_3(f)] \tag{8}$$

Thus, the DCM to map from the inertial frame to the Hill frame is equal to

$$[HN(\Omega, i, \omega, f)] = [HP][PN] = [M_3(f)][M_3(\omega)][M_1(i)][M_3(\Omega)] \tag{9}$$

2.2 Cartesian Coordinate Description

The relative position vector $\boldsymbol{\rho}$ of the deputy relative to the chief in Hill-frame components is

$${}^{\mathcal{H}}\boldsymbol{\rho} = \begin{bmatrix} x \\ y \\ z \end{bmatrix} \tag{10}$$

where the left superscript indicates that the vector is expressed in Hill frame $\mathcal{H}$ components, and x, y, z are the relative position coordinates in the Hill frame. In this frame, x and y describe the relative motion in the chief orbit plane while z describes any out-of-plane motion. Assuming a circular chief orbit (eccentricity $e = 0$) and small separation distances between the two spacecraft ($|\boldsymbol{\rho}| \ll |\boldsymbol{r}_c|$), the relative equations of motion (EOM) in the Hill frame are equal to [1]

$$\ddot{x} - 2n\dot{y} - 3n^2 x = 0 \tag{11}$$

$$\ddot{y} + 2n\dot{x} = 0 \tag{12}$$

$$\ddot{z} + n^2 z = 0 \tag{13}$$

These relative EOM are known as the Clohessy-Wiltshire-Hill (CWH) equations. Using the semi-major axis a of the chief orbit and the standard gravitational parameter μ of the central body, the mean motion n is determined by $n = \sqrt{\mu/a^3}$. The analytical solution to the CWH equations is equal to [40, 41]

$$x(t) = A_0 \cos(nt + \alpha) + x_{\text{off}} \tag{14}$$

$$y(t) = -2A_0 \sin(nt + \alpha) - \frac{3}{2} n t x_{\text{off}} + y_{\text{off}} \tag{15}$$

$$z(t) = B_0 \cos(nt + \beta) \tag{16}$$

with the velocities

$$\dot{x}(t) = -A_0 n \sin(nt + \alpha) \tag{17}$$

$$\dot{y}(t) = -2A_0 n \cos(nt + \alpha) - \frac{3}{2} n x_{\text{off}} \tag{18}$$

$$\dot{z}(t) = -B_0 n \sin(nt + \beta) \tag{19}$$

The six relative motion parameters in Eq. (14) are called the CW constants or linearized relative orbit elements (LROEs) and are the invariants of the linearized relative motion:

- In-plane sinusoidal amplitude A_0
- In-plane phase angle α
- Orbit-radial offset x_{off}
- Along-track offset at epoch y_{off}
- Out-of-plane sinusoidal amplitude B_0
- Out-of-plane phase angle β

The corresponding LROE state vector is

$$\delta \boldsymbol{\alpha e}_{CW} = [A_0 \quad \alpha \quad x_{\text{off}} \quad y_{\text{off}} \quad B_0 \quad \beta]^T \tag{20}$$

These geometrically insightful invariants of motion are determined through the initial conditions or cartesian state according to Eq. (111) and fully define the relative motion under the given assumptions.

Examining Eq. (14), one finds that the in-plane motion corresponds to a 2-by-1 ellipse in which the along-track amplitude is twice the orbit-radial amplitude, and the out-of-plane motion corresponds to an unforced oscillator. The motion may be offset in the *y*-direction with y_{off} or the *x*-direction with x_{off}. An offset x_{off} causes a drift in the along-track direction y over time due to the difference in semi-major axis of the two spacecraft. Thus, x_{off} must be zero for bounded motion. For a simple lead-follower formation, all relative motion parameters besides y_{off} are zero. Some relative orbit shapes in the Hill frame are shown in Fig. 4.

2.3 Orbit Element Difference Description

Given the general orbit elements

$$\boldsymbol{\alpha e} = [a \quad e \quad i \quad \Omega \quad \omega \quad M_0]^T \tag{21}$$

with semi-major axis *a*, eccentricity *e*, inclination *i*, right ascension of the ascending node Ω, argument of periapsis ω and initial mean anomaly M_0, the orbit element differences between the deputy and the chief spacecraft are equal to [27, 40]

$$\delta \boldsymbol{\alpha e} = \boldsymbol{\alpha e}_d - \boldsymbol{\alpha e}_c = [\delta a \quad \delta e \quad \delta i \quad \delta\Omega \quad \delta\omega \quad \delta M_0]^T \tag{22}$$

where $\boldsymbol{\alpha e}_d$ and $\boldsymbol{\alpha e}_c$ are the orbit elements of the deputy and chief, respectively. This differential orbit elements (DOEs) description does not make any assumptions on the

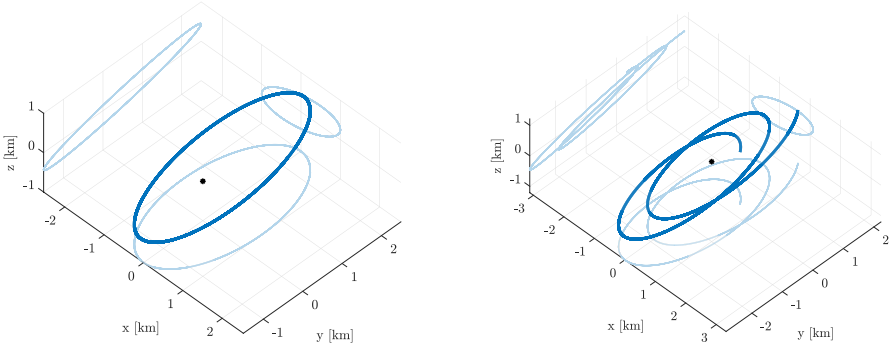

(a) Motion 1: $A_0 = 1$ km, $\alpha = -60$ deg, $x_{\text{off}} = 0$ km, $y_{\text{off}} = 0.5$ km, $B_0 = 0.5$ km, $\beta = 0$ deg

(b) Motion 2: $A_0 = 1$ km, $\alpha = -60$ deg, $x_{\text{off}} = 0.1$ km, $y_{\text{off}} = 0.5$ km, $B_0 = 0.5$ km, $\beta = 0$ deg

Fig. 4 Relative motion in Hill frame for a circular chief orbit: A_0 creates a 2-by-1 relative orbit ellipse that is offset in the y-direction by y_{off}. Drift motion is induced by x_{off}. The projections of the relative orbit on the three planes are shown in lighter color

eccentricity of the orbits. A semi-major axis difference δa between the two spacecraft causes the mean anomaly difference δM to drift over time. The relation between the differences in mean anomaly at time t and time t_0 is equal to

$$\delta M = \delta M_0 - \frac{3}{2}\frac{\delta a}{a}(M - M_0) \tag{23}$$

where M and M_0 are the mean anomalies of the chief at time t and time t_0, respectively. Assuming small relative orbit sizes, the relative position coordinates x, y, z can be expressed in terms of the orbit element differences and as a function of the chief true anomaly f for general orbit eccentricities [40, Chapter 14]

$$x(f) = \frac{r}{a}\delta a + \frac{ae\sin f}{\eta}\delta M - a\cos f\delta e \tag{24}$$

$$y(f) = \frac{r}{\eta^3}(1 + e\cos f)^2\delta M + r\delta\omega + \frac{r\sin f}{\eta^2}(2 + e\cos f)\delta e + r\cos i\delta\Omega \tag{25}$$

$$z(f) = r(\sin\theta\delta i - \cos\theta\sin i\delta\Omega) \tag{26}$$

with the relation $\eta = \sqrt{1 - e^2}$, the true latitude $\theta = \omega + f$ and the chief orbit radius

$$r = \frac{p}{1 + e\cos f} = \frac{a(1 - e^2)}{1 + e\cos f} = \frac{a\eta^2}{1 + e\cos f} \tag{27}$$

Note that most terms in Eq. (24) include the orbit radius r, which varies with true anomaly f for an elliptic chief orbit.

3 Circular Chief Orbits

3.1 Inertial Frame Relative Orbit Elements

First, the inertial relative motion is investigated for circular chief orbits using the Clohessy-Wiltshire equations. To express the relative motion in the inertial frame, the relative position $\boldsymbol{\rho}$ is mapped from the Hill frame $\mathcal{H}$ to the inertial frame $\mathcal{N}$ with the DCM $[NH] = [HN]^T$:

$$^{\mathcal{N}}\boldsymbol{\rho} = {}^{\mathcal{N}}\begin{bmatrix} X \\ Y \\ Z \end{bmatrix} = [NH] \cdot \ {}^{\mathcal{H}}\boldsymbol{\rho} = [HN]^T \cdot \ {}^{\mathcal{H}}\boldsymbol{\rho} \tag{28}$$

For general chief orbit elements (Ω, i, ω) and relative orbit parameters, this results in a rather complex analytical expression that is difficult to analyze. Thus, to begin, it assumed that $\Omega = i = \omega = 0$. This corresponds to a description in the perifocal frame $\mathcal{P}$:

$$^{\mathcal{P}}\boldsymbol{\rho} = {}^{\mathcal{P}}\begin{bmatrix} X_p \\ Y_p \\ Z_p \end{bmatrix} = [HN(0,0,0,f)]^T \cdot \ {}^{\mathcal{H}}\boldsymbol{\rho} = [HP]^T \cdot \ {}^{\mathcal{H}}\boldsymbol{\rho} \tag{29}$$

Once the relative motion is understood in the perifocal frame, it is rather straightforward to consider general chief orbit orientations. For a circular orbit, $f = nt$, so using Eqs. (14) and (29) as well as significant simplification results in the analytical expression

$$^{\mathcal{P}}\begin{bmatrix} X_p(t) \\ Y_p(t) \\ Z_p(t) \end{bmatrix} = {}^{\mathcal{P}}\begin{bmatrix} \frac{1}{2}\left(3A_0\cos\alpha - A_0\cos(\alpha+2nt) + 3ntx_{\text{off}}\sin(nt) + 2x_{\text{off}}\cos(nt) - 2y_{\text{off}}\sin(nt)\right) \\ \frac{1}{2}\left(-3A_0\sin\alpha - A_0\sin(\alpha+2nt) - 3ntx_{\text{off}}\cos(nt) + 2x_{\text{off}}\sin(nt) + 2y_{\text{off}}\cos(nt)\right) \\ B_0\cos(\beta+nt) \end{bmatrix} \tag{30}$$

Using the identities

$$A\sin t + B\cos t = \sqrt{A^2+B^2}\cos\left(t - \arctan\left(\frac{A}{B}\right)\right) \tag{31}$$

$$A\sin t + B\cos t = -\sqrt{A^2+B^2}\sin\left(t - \arctan\left(\frac{B}{-A}\right)\right) \tag{32}$$

and other well-known trigonometric identities, Eq. (30) is rewritten to significantly reduce its complexity:

$$X_p(t) = 3d_i\cos\alpha_i - d_i\cos(2nt-\alpha_i) - 2r_i\cos(nt-\phi_i) \tag{33}$$

$$Y_p(t) = 3d_i\sin\alpha_i - d_i\sin(2nt-\alpha_i) - 2r_i\sin(nt-\phi_i) \tag{34}$$

$$Z_p(t) = B_i \cos(nt - \beta_i) \tag{35}$$

Here, the inertial frame relative state vector

$$\delta\boldsymbol{\alpha e}_i = [r_i \quad \phi_i \quad d_i \quad \alpha_i \quad B_i \quad \beta_i]^T \tag{36}$$

is used, with

$$r_i = \frac{1}{2}\sqrt{\left(y_{\text{off}} - \frac{3}{2}ntx_{\text{off}}\right)^2 + x_{\text{off}}^2} \tag{37}$$

$$\phi_i = \arctan\left(\frac{y_{\text{off}} - \frac{3}{2}ntx_{\text{off}}}{-x_{\text{off}}}\right) \tag{38}$$

$$d_i = \frac{1}{2}A_0 \tag{39}$$

$$\alpha_i = -\alpha \tag{40}$$

$$B_i = B_0 \tag{41}$$

$$\beta_i = -\beta \tag{42}$$

Ignoring the constant offset of $3d_i$ as well as the phase angles ϕ_i and α_i, the equations for X_p and Y_p are equivalent to the parametric equations of an epitrochoid.[1] An epitrochoid is the curve traced by a point attached to a circle rolling around the outside of a fixed circle without slip. In the case of Eq. (33), the radius of both circles is equal to r_i, and the distance between the generating point and the center of the rolling circle is equal to the arm length d_i. The fixed circle is offset by $3d_i$ away from the frame origin (the chief). The phase angle α_i rotates the epitrochoid curve around the $\hat{\boldsymbol{p}}_3$ axis, and ϕ_i is a phase offset of the rolling circle. The phase offset ϕ_i is equal to $\phi_i = \pm\frac{\pi}{2}$ unless $x_{\text{off}} \neq 0$. Drift motion through an orbit-radial offset x_{off} changes the radius r_i of the circles and the phase offset ϕ_i over time. That is, only r_i and ϕ_i are time-varying if the orbit-radial offset x_{off} is non-zero. The Z_p motion corresponds to a simple unforced oscillator with amplitude B_i and phase angle β_i, as is the case for the CWH Eq. (14) in the Hill frame.

Similar to the elliptic relative orbit shape in the Hill frame, the epitrochoid-based formulation provides an intuitive description of the relative motion in the perifocal frame and consequently the inertial frame, as shown in Fig. 5. The six inertial frame relative orbit elements (IROEs) in Eq. (37) are

- Circle radius r_i

[1] see https://en.wikipedia.org/wiki/Epitrochoid. The equations only differ by a phase offset $\theta = \pi/2 - nt$ and are mirrored with $x = -X_p$. (Consulted on: 05/23/2025).

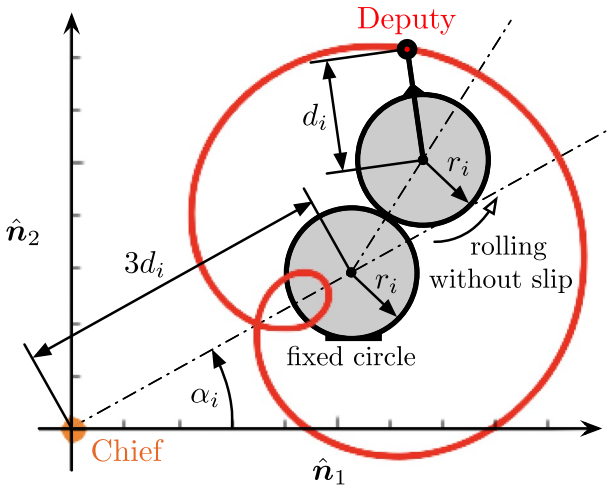

Fig. 5 Inertial frame relative orbit elements: The relative motion in the inertial frame traces an epitrochoid curve, in which a circle with radius r_i rolls without slip on a fixed circle with radius r_i, and the curve is generated by a point that is at a distance of d_i away from the center of the rolling circle. The formation is $3d_i$ away from the origin and rotated by α_i

- Phase offset of rolling circle ϕ_i
- Arm length d_i
- In-plane rotation α_i
- Out-of-plane sinusoidal amplitude B_i
- Out-of-plane phase angle β_i

The inverse mapping of Eq. (37) is derived in Appendix 2 and is given by

$$A_0 = 2d_i \tag{43}$$

$$\alpha = -\alpha_i \tag{44}$$

$$x_{\text{off}} = -2r_i \cos\phi_i \tag{45}$$

$$y_{\text{off}} = 2r_i \left(\sin\phi_i - \frac{3}{2} nt \cos\phi_i \right) \tag{46}$$

$$B_0 = B_i \tag{47}$$

$$\beta = -\beta_i \tag{48}$$

To obtain the velocity states, the time derivatives of r_i and ϕ_i are derived first. Because x_{off} and y_{off} are constants, the time derivatives of Eqs. (45) and (46) are equal to

$$0 = -\dot{r}_i \cos\phi_i + r_i \sin\phi_i \dot{\phi}_i \tag{49}$$

and

$$0 = \dot{r}_i \left(\sin\phi_i - \frac{3}{2} nt \cos\phi_i \right) + r_i \left(\cos\phi_i \dot{\phi}_i - \frac{3}{2} n \cos\phi_i + \frac{3}{2} nt \sin\phi_i \dot{\phi}_i \right) \tag{50}$$

Solving these two equations for $\dot{r}_i$ and $\dot{\phi}_i$ yields

$$\dot{r}_i = \frac{3}{2} r_i n \cos\phi_i \sin\phi_i = \frac{3}{4} r_i n \sin(2\phi_i) \tag{51}$$

and

$$\dot{\phi}_i = \frac{3}{2} n \cos^2\phi \tag{52}$$

Taking the time derivative of Eq. (33) and substituting Eqs. (51) and (52) gives the velocity states in the perifocal frame in terms of the IROEs:

$$\dot{X}_p(t) = 2 d_i n \sin(2nt - \alpha_i) + \frac{1}{2} r_i n \big(\sin(nt - \phi_i) - 3 \sin(nt + \phi_i) \big) \tag{53}$$

$$\dot{Y}_p(t) = -2 d_i n \cos(2nt - \alpha_i) - \frac{1}{2} r_i n \big(\cos(nt - \phi_i) - 3 \cos(nt + \phi_i) \big) \tag{54}$$

$$\dot{Z}_p(t) = -B_i n \sin(nt - \beta_i) \tag{55}$$

The same relative orbits as in Fig. 4 are shown in Fig. 6 in the inertial frame.

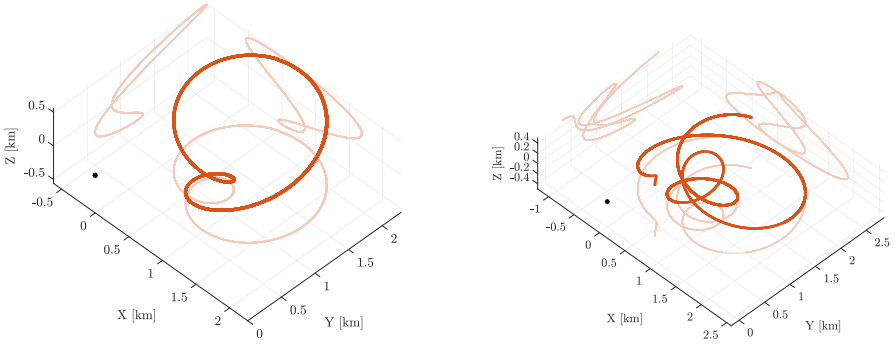

(a) Motion 1: $A_0 = 1$ km, $\alpha = -60$ deg, $x_{\text{off}} = 0$ km, $y_{\text{off}} = 0.5$ km, $B_0 = 0.5$ km, $\beta = 0$ deg

(b) Motion 2: $A_0 = 1$ km, $\alpha = -60$ deg, $x_{\text{off}} = 0.1$ km, $y_{\text{off}} = 0.5$ km, $B_0 = 0.5$ km, $\beta = 0$ deg

Fig. 6 Relative motion in Inertial frame: The in-plane motion corresponds to an epitrochoid curve. The projections of the relative orbit on the three planes are shown in lighter color

3.2 General Chief Orbit Orientation

In Eq. (33), the relative motion is described in the perifocal frame, which corresponds to the inertial frame only if $\Omega = i = \omega = 0$. However, the derived inertial relative orbit elements are considered to be the relevant parameters for the inertial frame relative motion, because for general chief orbit elements only the orientation of the relative orbit changes, but not the shape. Unlike the transition from the Hill frame $\mathcal{H}$ to the perifocal frame $\mathcal{P}$, which results in a general change of the relative orbit shape, the mapping from the perifocal frame $\mathcal{P}$ to the inertial frame $\mathcal{N}$ is straightforward as it is a pure rotation. The effect of the chief orbit orientation due to (Ω, i, ω) on the orientation of the inertial frame relative orbit is illustrated in Fig. 7.

3.3 Invariants of Motion

The inertial frame relative orbit elements provide an intuitive way of describing the relative motion in the inertial frame. However, two of the elements, r_i and ϕ_i, are time-varying if the orbit-radial offset x_{off} is non-zero. To obtain the invariants of motion in the inertial frame that are constant in time, r_i and ϕ_i are evaluated at epoch $t = 0$. This yields

$$r_{i,0} = \frac{1}{2}\sqrt{y_{\text{off}}^2 + x_{\text{off}}^2} \tag{56}$$

and

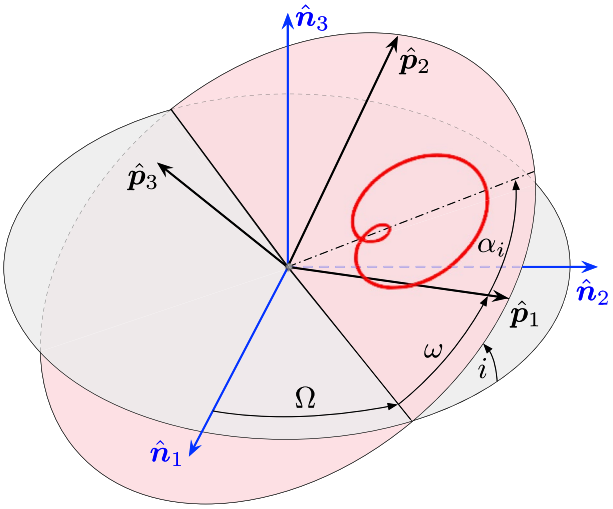

Fig. 7 Effect of chief orbit orientation (Ω, i, ω) on inertial frame relative motion: the relative motion may be conveniently described in the perifocal frame, as the mapping from perifocal frame to inertial frame is a pure rotation

$$\phi_{i,0} = \arctan\left(\frac{y_{\text{off}}}{-x_{\text{off}}}\right) \tag{57}$$

to make up the time-invariant inertial relative state vector

$$\delta\boldsymbol{\alpha e}_{i,0} = [r_{i,0} \quad \phi_{i,0} \quad d_i \quad \alpha_i \quad B_i \quad \beta_i]^T \tag{58}$$

To relate the general elements r_i and ϕ_i to the inertial frame invariants $r_{i,0}$ and $\phi_{i,0}$, Eqs. (45) and (46) are also evaluated at $t = 0$

$$x_{\text{off}} = -2r_{i,0}\cos\phi_{i,0} \tag{59}$$

$$y_{\text{off}} = 2r_{i,0}\sin\phi_{i,0} \tag{60}$$

and substituted into Eqs. (37) and (38) to give

$$r_i = r_{i,0}\sqrt{1 + 3nt\cos\phi_{i,0}\left(\sin\phi_{i,0} + \frac{3}{4}nt\cos\phi_{i,0}\right)} \tag{61}$$

and

$$\phi_i = \arctan\left(\tan\phi_{i,0} + \frac{3}{2}nt\right) \tag{62}$$

This allows to directly propagate r_i and ϕ_i in time given an initial radius $r_{i,0}$ and phase offset $\phi_{i,0}$. If $\phi_{i,0} = \pm\frac{\pi}{2}$, then r_i and ϕ_i are constant in time and no drift motion occurs. Substituting Eqs. (61) and (62) into Eqs. (33) and (53) yields the position

$$X_p(t) = 3d_i\cos\alpha_i - d_i\cos(2nt - \alpha_i) - 2r_{i,0}\left(\cos(nt - \phi_{i,0}) + \frac{3}{2}nt\sin(nt)\cos\phi_{i,0}\right) \tag{63}$$

$$Y_p(t) = 3d_i\sin\alpha_i - d_i\sin(2nt - \alpha_i) - 2r_{i,0}\left(\sin(nt - \phi_{i,0}) - \frac{3}{2}nt\cos(nt)\cos\phi_{i,0}\right) \tag{64}$$

$$Z_p(t) = B_i\cos(nt - \beta_i) \tag{65}$$

and velocity

$$\dot{X}_p(t) = 2d_i n\sin(2nt - \alpha_i) + \frac{1}{2}r_{i,0}n\big(\sin(nt - \phi_{i,0}) - 3\sin(nt + \phi_{i,0}) - 6nt\cos(nt)\cos\phi_{i,0}\big) \tag{66}$$

$$\begin{aligned}\dot{Y}_p(t) = {} & -2d_i n\cos(2nt - \alpha_i) - \frac{1}{2}r_{i,0}n\big(\cos(nt - \phi_{i,0}) - 3\cos(nt + \phi_{i,0}) \\ & + 6nt\sin(nt)\cos\phi_{i,0}\big)\end{aligned} \tag{67}$$

$$\dot{Z}_p(t) = -B_i n \sin(nt - \beta_i) \tag{68}$$

in the inertial frame in terms of the time-invariant IROEs.

3.4 Closed Relative Orbits

For a closed relative orbit (no drift motion), the orbit-radial offset in the CW equations must be zero, i.e. $x_{\text{off}} = 0$. This results in $\phi_i = \phi_{i,0} = \pm\frac{\pi}{2}$ and $r_i = r_{i,0}$. The shape and size of the inertial frame relative orbit are determined by r_i and d_i. Figure 8 shows inertial frame relative orbits for several different values of r_i and d_i, with all remaining IROEs equal to zero. If $r_i = 0$, the relative orbit shape is circular. The target completes two revolutions of this circle during one orbital period. This is more clear when r_i is slightly increased from 0 to 0.1, where an inner loop becomes visible. Increasing r_i causes the relative orbit size to grow, while the inner loop becomes smaller. The inner loop disappears when $r_i = d_i$. Increasing r_i even more makes the relative orbit shape more circular. If $d_i = 0$, the relative orbit is circular and centered at the chief, with one revolution per orbital period.

As mentioned in Sect. 3.1, the relative orbit is offset from the chief by a distance of $3d_i$. Increasing r_i increases the relative orbit size due to the greater size of the circles that generate the epitrochoid curve. The ratio of r_i and d_i determines the shape of the relative orbit. If $r_i < d_i$, the generating point is outside the rolling circle, creating an inner loop. If $r_i = d_i$, the generating point is on the surface of the rolling circle, creating a cusp. Finally, if $r_i > d_i$, the generating point is inside the rolling circle, creating a curve that becomes circular as $d_i \to 0$. If $r_i > 2d_i$, the deputy circumnavigates the chief, and if $r_i < 2d_i$, the deputy remains on one inertial side of the chief.

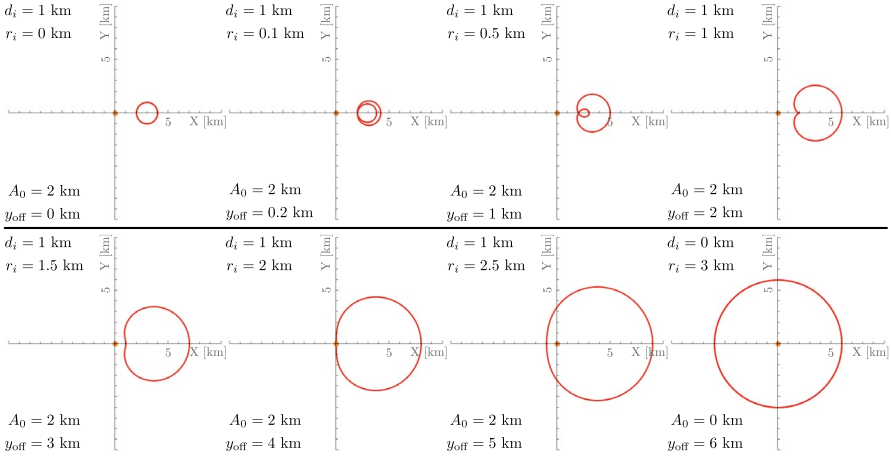

Fig. 8 Inertial frame relative orbits for circular chief orbits: The size of the relative orbit changes with r_i, while the shape changes with the ratio of r_i and d_i

3.5 Drift Motion

An orbit-radial offset x_{off}, resulting in $\phi_{i,0} \neq \frac{\pi}{2}$, causes drift of the deputy with respect to the chief due to the difference in semi-major axis of the two spacecraft that leads to different orbital periods. In the Hill frame, the drift motion occurs in the x-direction. In the inertial frame, the drift motion results in a change of the circle radius r_i and the in-plane phase offset ϕ_i over time. Such inertial frame drift motion is shown in Fig. 9. Because r_i changes while d_i remains constant, the shape (inner loop, cusp, no loop) of the epitrochoid changes over time as well.

4 Elliptic Chief Orbits

The Clohessy-Wilsthire equations assume a circular chief orbit and are not applicable to general chief orbit eccentricities. For elliptic chief orbits, the orbit element difference description is more appropriate. Using Eqs. (24) and (29) results after several simplification steps in the analytical expression

$$
{}^{\mathcal{P}}\begin{bmatrix} X_p(f) \\ Y_p(f) \\ Z_p(f) \end{bmatrix} = {}^{\mathcal{P}}\begin{bmatrix} r\left(\frac{\delta a \cos f}{a} - \frac{\delta e(2e\cos f - \cos(2f) + 3)}{2\eta^2} - \frac{\delta M(\sin f + e \sin f \cos f)}{\eta^3} - \delta\omega \sin f - \delta\Omega \cos i \sin f\right) \\ r\left(\frac{\delta a \sin f}{a} + \frac{\delta e \sin(2f)}{2\eta^2} + \delta M \frac{2(1+e^2)\cos f + e\cos(2f) + 3e}{2\eta^3} + \delta\omega \cos f + \delta\Omega \cos i \cos f\right) \\ r\left(\delta i \sin\theta - \delta\Omega \sin i \cos\theta\right) \end{bmatrix} \tag{69}
$$

Similar to the inertial frame transformation for circular chief orbits, Eq. (31) is used to rewrite and simplify Eq. (69):

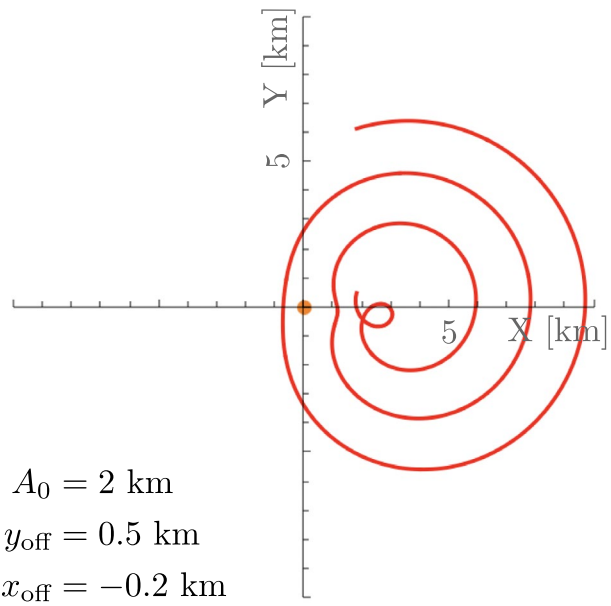

Fig. 9 Drift motion in the inertial frame: An offset x_{off} causes the radius r_i to change over time

$$X_p(f) = \frac{\eta^2}{1+e\cos f}\left((3+2e\cos f)d_i\cos\alpha_i - d_i\cos(2f-\alpha_i) - 2r_i\cos(f-\phi_i)\right) \quad (70)$$

$$Y_p(f) = \frac{\eta^2}{1+e\cos f}\left((3+2e\cos f)d_i\sin\alpha_i - d_i\sin(2f-\alpha_i) - 2r_i\sin(f-\phi_i)\right) \quad (71)$$

$$Z_p(f) = \frac{\eta^2}{1+e\cos f}B_i\cos(\omega+f-\beta_i) \quad (72)$$

Aside from the $2e\cos f$ term and the formulation as function of true anomaly f instead of time t, the form of these equations is the same as in Eq. (33). All components are multiplied by the chief orbit radius r, which is a function of f. For elliptic chief orbits and the differential orbit elements description, the inertial frame relative orbit elements are determined by

$$r_i = \frac{a}{2}\sqrt{\left(\frac{1}{\eta^3}\delta M + \cos i\delta\Omega + \delta\omega\right)^2 + \left(\frac{\delta a}{a}\right)^2} \quad (73)$$

$$\phi_i = \arctan\left(\frac{\frac{1}{\eta^3}\delta M + \cos i\delta\Omega + \delta\omega}{-\frac{\delta a}{a}}\right) \quad (74)$$

$$d_i = \frac{a}{2\eta^3}\sqrt{(\eta\delta e)^2 + (e\delta M)^2} \quad (75)$$

$$\alpha_i = \arctan\left(\frac{e\delta M}{-\eta\delta e}\right) \quad (76)$$

$$B_i = a\sqrt{\delta i^2 + (\sin i\delta\Omega)^2} \quad (77)$$

$$\beta_i = \arctan\left(\frac{\delta i}{-\sin i\delta\Omega}\right) \quad (78)$$

Note that several of these IROEs are a function of the same differential orbital elements. However, if one wants to specify d_i and α_i, for example, and determine the values for δe and δM that result in these specified parameters, it is rather straightforward to substitute one equation into the other and solve for δe and δM. The inverse mapping for Eq. 73 is provided in Eq. 134 in Appendix 3. For $e = 0$, this differential orbit element description may be used for the circular chief orbit relative motion.

Figure 10 shows various closed inertial frame relative orbits for an elliptic chief orbit with eccentricity of $e = 0.5$ and semi-major axis of $a = 10000$ km. For the DOE description, δe is similar to the in-plane amplitude A_0 for the circular chief orbit, while $\delta\omega$ is similar to the along-track offset y_{off}. An eccentric orbit essentially stretches part of the 2-by-1 relative orbit ellipse in the Hill frame in the y-direction. This is due to the dependence of the relative motion on the chief orbit radius r, which

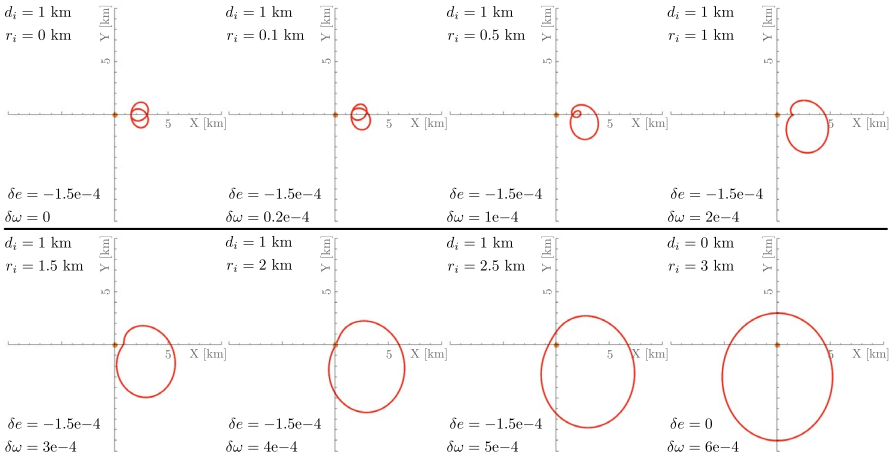

Fig. 10 Inertial frame relative orbits for elliptic chief orbits: The relative orbit is stretched for elliptic chief orbits

is the greatest at apoapsis. The part of the Hill frame relative orbit ellipse that is stretched the most in the y-direction corresponds to the part that is traversed while the spacecraft are on the apoapsis side of the orbit. This is visible for the inertial frame relative orbits in Fig. 10 as well. For $\delta e = -0.00015$, the inertial frame relative orbit is stretched equally in the $-Y_p$ and $+Y_p$ direction. For a positive $\delta\omega$ the relative orbit stretches more in the $-Y_p$ direction. This is because the $\delta\omega$ offset shifts the relative orbit in the $+y$ direction of the Hill frame and stretches the orbit more in the $+y$ direction than the $-y$ direction. This stretched part of the relative orbit is traversed when the $+y$ direction of the Hill frame is pointing in the $-Y_p$ direction of the perifocal frame, resulting in a larger relative orbit part in $-Y_p$. Similar to the circular chief orbit case, increasing r_i while d_i remains the same causes the inner loop to disappear and turn into a cusp when $r_i = d_i$. Increasing r_i further such that $r_i > d_i$ makes the inertial frame relative orbit more and more elliptic. If $d_i = 0$, the relative orbit is elliptic in the inertial frame.

An example for the inertial frame orbit rotation for an elliptic chief orbit is shown in Fig. 11. To induce a rotation of α_i, the ratio of $(e\delta M)/(-\eta\delta e)$ must be changed. To maintain the same d_i, $e\delta M$ and $-\eta\delta e$ cannot be arbitrarily changed, however, and $\delta\omega$ must be adjusted as well such that r_i remains the same. Thus, the relative orbit shape changes when a rotation of α_i is applied.

The effect of the chief orbit orientation (Ω, i, ω) on the relative orbit shape in the perifocal frame is already considered in Eq. (70). The remaining rotation of the relative orbit through (Ω, i, ω) is the same for the elliptic orbit as for the circular orbit, as illustrated in Fig. 7.

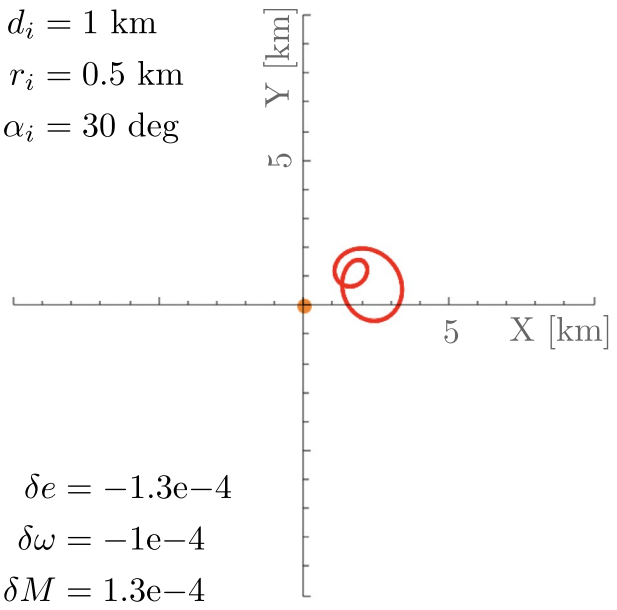

Fig. 11 Rotation of inertial frame relative orbit for elliptic chief orbits: a rotation by α_i also changes the relative orbit shape

5 Control Development

The relative orbits discussed in the previous sections assume no perturbations. This section develops the inertial relative orbit element variational equations which allow orbit environment or control perturbations to be considered. A continuous-time feedback control law based on the inertial frame relative orbit elements is developed as an illustration on how this new formulation readily enables maintaining a certain inertial relative orbit despite perturbations, and to allow for re-configurations from one formation to another.

5.1 Variational Equations

The Lagrangian-bracket methodology is applied here to derive the variational equations, which show how the invariants of the unperturbed motion change in time due to perturbing accelerations. To aid readability, the δ notation to indicate a relative orbit element set is dropped, i.e. $\boldsymbol{oe}_i$ is used instead of $\delta\boldsymbol{oe}_i$. Moreover, all quantities are expressed in the perifocal frame $\mathcal{P}$, so $\boldsymbol{\rho}$ is written instead of ${}^{\mathcal{P}}\boldsymbol{\rho}$, for example. The time-invariant IROE set

$$\boldsymbol{oe}_{i,0} = [r_{i,0} \quad \phi_{i,0} \quad d_i \quad \alpha_i \quad B_i \quad \beta_i]^T \tag{79}$$

changes in time according to [40, Chapter 12]

$$\dot{\boldsymbol{\alpha}}_{i,0} = [L]^{-1} \left[\frac{\partial \boldsymbol{\rho}}{\partial \boldsymbol{\alpha}_{i,0}} \right]^T \boldsymbol{a}_p \tag{80}$$

where $[L]$ is the Lagrangian-bracket matrix, $\boldsymbol{\rho}$ is the relative position vector, and $\boldsymbol{a}_p$ is the perturbing acceleration. Using the matrix

$$[J] = \begin{bmatrix} 0_{3\times3} & I_{3\times3} \\ -I_{3\times3} & 0_{3\times3} \end{bmatrix} \tag{81}$$

and the cartesian state in the perifocal frame

$$\boldsymbol{s}_p(t, \boldsymbol{\alpha}_{i,0}) = \begin{bmatrix} X_p & Y_p & Z_p & \dot{X}_p & \dot{Y}_p & \dot{Z}_p \end{bmatrix}^T \tag{82}$$

the Lagrangian-bracket matrix is computed by

$$[L] = \frac{\partial \boldsymbol{s}_p}{\partial \boldsymbol{\alpha}_{i,0}}^T [J] \frac{\partial \boldsymbol{s}_p}{\partial \boldsymbol{\alpha}_{i,0}} \tag{83}$$

or element-wise via

$$L_{ij} = [\alpha_i, \alpha_j] = \left(\frac{\partial \boldsymbol{\rho}}{\partial \alpha_i} \right)^T \frac{\partial \dot{\boldsymbol{\rho}}}{\partial \alpha_j} - \left(\frac{\partial \dot{\boldsymbol{\rho}}}{\partial \alpha_i} \right)^T \frac{\partial \boldsymbol{\rho}}{\partial \alpha_j} \tag{84}$$

where $\dot{\boldsymbol{\rho}}$ is the relative velocity vector and α_i and α_j are the i-th and j-th element of the relative orbit element set $\boldsymbol{\alpha}_{i,0}$, respectively. The partials are obtained by taking the derivative of Eqs. (63) and (66) with respect to the relative orbit elements $\boldsymbol{\alpha}_{i,0}$. By defining

$$[B] = [L]^{-1} \left[\frac{\partial \boldsymbol{\rho}}{\partial \boldsymbol{\alpha}_{i,0}} \right]^T \tag{85}$$

the equations of motion of the IROE set $\boldsymbol{\alpha}_{i,0}$ are compactly written as

$$\dot{\boldsymbol{\alpha}}_{i,0} = [B] \boldsymbol{a}_p \tag{86}$$

These linearized relative motion variational equations describe how a perturbing acceleration changes the osculating inertial frame relative orbit elements over time. Taking the partials of $\boldsymbol{\rho}$ in Eq. (63) and $\dot{\boldsymbol{\rho}}$ in Eq. (66) with respect to the IROE set $\boldsymbol{\alpha}_{i,0}$, yields the corresponding Lagrangian-bracket matrix

$$[L]_{i,0} = \begin{bmatrix} 0 & 2r_{i,0}n & 0 & 0 & 0 & 0 \\ -2r_{i,0}n & 0 & 0 & 0 & 0 & 0 \\ 0 & 0 & 0 & 4d_i n & 0 & 0 \\ 0 & 0 & -4d_i n & 0 & 0 & 0 \\ 0 & 0 & 0 & 0 & 0 & B_i n \\ 0 & 0 & 0 & 0 & -B_i n & 0 \end{bmatrix} \tag{87}$$

Taking the inverse of Eq. (87) and multiplying with the partial of the relative position $\boldsymbol{\rho}$ w.r.t. the relative orbit element set $\boldsymbol{\alpha e}_{i,0}$ gives

$$[B]_{i,0} = \begin{bmatrix} -\frac{-2\sin(nt-\phi_{i,0})+3nt\sin(\phi_{i,0})\sin(nt)}{2n} & \frac{-2\cos(nt-\phi_{i,0})+3nt\sin(\phi_{i,0})\cos(nt)}{2n} & 0 \\ -\frac{2\cos(nt-\phi_{i,0})+3nt\cos(\phi_{i,0})\sin(nt)}{2nr_{i,0}} & \frac{-2\sin(nt-\phi_{i,0})+3nt\cos(\phi_{i,0})\cos(nt)}{2nr_{i,0}} & 0 \\ \frac{\sin(2nt-\alpha_i)+3\sin(\alpha_i)}{4n} & -\frac{\cos(2nt-\alpha_i)+3\cos(\alpha_i)}{4n} & 0 \\ \frac{-\cos(2nt-\alpha_i)+3\cos(\alpha_i)}{4d_i n} & \frac{-\sin(2nt-\alpha_i)+3\sin(\alpha_i)}{4d_i n} & 0 \\ 0 & 0 & \frac{-\sin(nt-\beta_i)}{n} \\ 0 & 0 & \frac{\cos(nt-\beta_i)}{B_i n} \end{bmatrix} \tag{88}$$

This matrix may be used to directly relate the variation of the inertial frame relative orbit elements to perturbations in the perifocal frame. Note that the rows corresponding to $\dot{\phi}_{i,0}$, $\dot{\alpha}_i$ and $\dot{\beta}_i$ are singular if $r_{i,0}$, d_i or B_i are zero, respectively. Thus, while the IROE set derived in Sect. 3.1 is illustrative, it is not necessarily the best for control purposes. Instead, an alternative non-singular IROE set is introduced

$$\boldsymbol{\alpha e}_{i,0,ns} = [R_{1,0} \quad R_{2,0} \quad D_1 \quad D_2 \quad B_1 \quad B_2]^T \tag{89}$$

where the relative orbit elements are similar to the LROE set proposed in Ref. [26]:

$$R_{1,0} = r_{i,0}\cos\phi_{i,0} \tag{90}$$

$$R_{2,0} = r_{i,0}\sin\phi_{i,0} \tag{91}$$

$$D_1 = d_i\cos\alpha_i \tag{92}$$

$$D_2 = d_i\sin\alpha_i \tag{93}$$

$$B_1 = B_i\cos\beta_i \tag{94}$$

$$B_2 = B_i\sin\beta_i \tag{95}$$

For this $\boldsymbol{\alpha e}_{i,0,ns}$ set, the Lagrangian-bracket matrix $[L]$ is equal to

$$[L]_{i,0,ns} = \begin{bmatrix} 0 & 2n & 0 & 0 & 0 & 0 \\ -2n & 0 & 0 & 0 & 0 & 0 \\ 0 & 0 & 0 & 4n & 0 & 0 \\ 0 & 0 & -4n & 0 & 0 & 0 \\ 0 & 0 & 0 & 0 & 0 & n \\ 0 & 0 & 0 & 0 & -n & 0 \end{bmatrix} \tag{96}$$

and the non-singular IROE variational equation $[B]$ matrix is equal to

$$[B]_{i,0,ns} = \begin{bmatrix} \frac{\sin(nt)}{n} & -\frac{\cos(nt)}{n} & 0 \\ -\frac{\cos(nt)+\frac{3}{2}nt\sin(nt)}{n} & \frac{-\sin(nt)+\frac{3}{2}nt\cos(nt)}{n} & 0 \\ \frac{\sin(2nt)}{4n} & -\frac{\cos(2nt)+3}{4n} & 0 \\ \frac{-\cos(2nt)+3}{4n} & -\frac{\sin(2nt)}{4n} & 0 \\ 0 & 0 & -\frac{\sin(nt)}{n} \\ 0 & 0 & \frac{\cos(nt)}{n} \end{bmatrix} \tag{97}$$

In this case, the denominators do not go to zero for any relative orbit elements, yielding non-singular variational equations. Moreover, note that in contrast to Eq. (88), this $[B]$ matrix does not depend on the IROEs, but only on the mean motion n and time t.

5.2 Continuous Feedback Control

A Lyapunov-based continuous feedback control law is developed to allow for station-keeping around a desired reference inertial frame orbit as well as reconfigurations from one formation to another. The deputy spacecraft (servicer) is assumed to be controlled, essentially replacing the perturbing acceleration $\boldsymbol{a}_p$ in Eq. (86) with the control acceleration $\boldsymbol{u}$. The difference between the osculating inertial frame relative orbit elements and the desired reference orbit elements corresponds to the IROE tracking error

$$\Delta\boldsymbol{oe}_i = \boldsymbol{oe}_i - \boldsymbol{oe}_{i,r} \tag{98}$$

where $\boldsymbol{oe}_i$ is used as a placeholder for either time-invariant IROE set described in Sect. 5.1, and $\boldsymbol{oe}_{i,r}$ is the corresponding reference IROE state. Taking the time-derivative and substituting Eq. (86) with the corresponding control vectors gives

$$\Delta\dot{\boldsymbol{oe}}_i = \dot{\boldsymbol{oe}}_i - \dot{\boldsymbol{oe}}_{i,r} = [B](\boldsymbol{u} - \boldsymbol{u}_r) \tag{99}$$

where $\boldsymbol{u}_r$ is a reference control vector allowing for a time-varying reference IROE state $\boldsymbol{oe}_{i,r} = \boldsymbol{oe}_{i,r}(t)$ [26]. Similar to the Lyapunov-based control development for mean orbit element differences [27] and the Hill frame non-singular orbit elements [26], the positive definite Lyapunov candidate function

$$V(\Delta\boldsymbol{oe}_i) = \frac{1}{2}\Delta\boldsymbol{oe}_i^T[K]\Delta\boldsymbol{oe}_i \tag{100}$$

is used, where $[K]$ is a 6×6 symmetric positive definite gain matrix. Taking the time derivative of the Lyapunov candidate function and substituting Eq. (99) yields

$$\dot{V}(\Delta\boldsymbol{oe}_i) = \Delta\boldsymbol{oe}_i^T[K][B](\boldsymbol{u} - \boldsymbol{u}_r) \tag{101}$$

Setting the Lyapunov rate $\dot{V}$ equal to the negative definite function

$$\dot{V}(\Delta\boldsymbol{\alpha e}_i) = -\Delta\boldsymbol{\alpha e}_i^T[K][K]\Delta\boldsymbol{\alpha e}_i \tag{102}$$

gives

$$[B](\boldsymbol{u} - \boldsymbol{u}_r) = -[K]\Delta\boldsymbol{\alpha e}_i \tag{103}$$

Taking the least-squares inverse of $[B]$ yields the control law

$$\boldsymbol{u} = \boldsymbol{u}_r - ([B]^T[B])^{-1}[B]^T[K]\Delta\boldsymbol{\alpha e}_i \tag{104}$$

and the resulting Lyapunov rate

$$\dot{V}(\Delta\boldsymbol{\alpha e}_i) = -\Delta\boldsymbol{\alpha e}_i^T[K][B]([B]^T[B])^{-1}[B]^T[K]\Delta\boldsymbol{\alpha e}_i = -\boldsymbol{y}^T([B]^T[B])^{-1}\boldsymbol{y} \tag{105}$$

with $\boldsymbol{y} = [B]^T[K]\Delta\boldsymbol{\alpha e}_i$. To guarantee Lyapunov stability, the Lyapunov rate must be negative semi-definite, and for asymptotic stability it must be negative definite. For the $\boldsymbol{\alpha e}_{i,0,ns}$ set, the matrix $([B]^T[B])^{-1}$ is symmetric and has only positive eigenvalues, so it is positive definite. Thus, the Lyapunov rate is semi-definite and the control is stabilizing. For asymptotic stability, the Lyapunov rate, and thus $\boldsymbol{y}$, must only be zero if the IROE tracking error $\Delta\boldsymbol{\alpha e}_i$ is zero. Because the $[B]$ matrix changes with time, there may be instances when $\boldsymbol{y}$ becomes zero while $\Delta\boldsymbol{\alpha e}_i$ is non-zero. However, this occurs only for an instant, as the $[B]$ matrix keeps changing as the two spacecraft orbit the central body. The largest invariant set in which $\boldsymbol{y}$ remains zero for all time corresponds to $\Delta\boldsymbol{\alpha e}_i = 0$. Consequently, the control is asymptotically stabilizing according to LaSalle's invariance principle.

5.3 Control Application

The control law developed in Sect. 5.2 is tested here using the initial and desired inertial relative orbit elements shown in Table 1. The non-singular time-invariant IROE set from Eq. (89) with corresponding $[B]$ matrix from Eq. (97) is used with the gain matrix.

$$[K]_{i,0,ns} = n \cdot \mathrm{diag}([30, 1, 0.5, 0.5, 1, 1]) \tag{106}$$

Because all elements of the $\boldsymbol{\alpha e}_{i,0,ns}$ set have the same unit, the feedback gain matrix is much easier to tune than they would be with the IROE set from Eq. (79). A higher feedback gain is chosen for the element corresponding to drift motion to quickly reduce drift. Given the cartesian relative state, the IROE state is computed with Eq. (140) and (90) in the control algorithm. The results are shown in Fig. 12. The rela-

Table 1 Initial and desired inertial frame relative orbit elements

	$r_{i,0}$ [m]	$\phi_{i,0}$ [deg]	d_i [m]	α_i [deg]	B_i [m]	β_i [deg]
Initial	304.138	99.462	300	0	10	−5.730
Desired	850	90	650	90	100	45

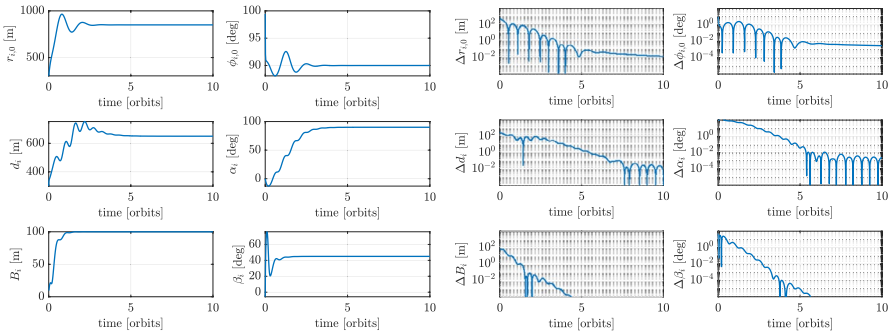

(a) Inertial frame relative orbit elements (b) Inertial frame relative orbit element errors

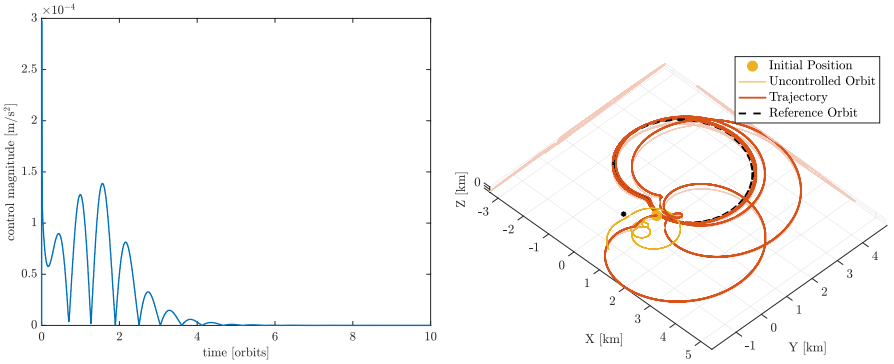

(c) Control magnitude (d) Inertial frame relative orbit

Fig. 12 Control of non-singular inertial frame relative orbit element set $\boldsymbol{\alpha}_{i,0,ns}$

tive orbit successfully converges to the desired relative orbit (Figs. 12a and 12b). Because the $[B]$ matrix is non-singular, this control description is also suitable for relative orbits with $r_{i,0}$, d_i or B_i equal to zero. The total Delta-V with this IROE set is $\Delta V = 2.0$ m/s.

6 Application to On-Orbit Servicing

The inertial frame relative orbit element description is used to design a relative orbit that satisfies inertially fixed keep-out constraints imposed by a cislunar plasma-wake. As explained in Sect. 1, the plasma wakes in cislunar space are assumed to be fixed in the inertial frame. However, the following application may be used for other general inertially fixed constraints such as to avoid eclipsing. This plasma wake is modeled as a keep-out cylinder that extends in the $\hat{\boldsymbol{n}}_1$ direction with a radius of $r_c = 10$ m, and the chief orbit elements are equal to $[a,\ e,\ i,\ \Omega,\ \omega,\ M_0]^T = [10000\text{ km},\ 0,\ 0\ 0\ 0\ 0]^T$. To remain outside the plasma wake keep-out zone, the servicer must maintain a minimum distance of $r_c = 10$ m from the cylinder axis. As can be seen in Fig. 5, this requires a rotation by α_i, as the relative orbit intersects the $\hat{\boldsymbol{n}}_1$ axis multiple times for $\alpha_i = 0$. To achieve the minimal distance, r_i and d_i must then be chosen accordingly.

The epitrochoid frame $\mathcal{E}: \{\hat{\boldsymbol{e}}_1, \hat{\boldsymbol{e}}_2, \hat{\boldsymbol{e}}_3\}$ is defined as the frame in which the orientation of the epitrochoid-shaped relative orbit is constant, with $[EP(\alpha_i)] = [M_3(\alpha_i)]$. That is, for $\alpha_i = 0$, the epitrochoid frame $\mathcal{E}$ corresponds to the perifocal frame $\mathcal{P}$, and otherwise it is obtained by rotating the frame $\mathcal{P}$ by α_i around the $\hat{\boldsymbol{p}}_3$ axis. The solution in the epitrochoid frame is obtained by setting $\alpha_i = 0$ in Eq. (33). For a closed orbit ($\phi_i = \frac{\pi}{2}$), this gives

$$X_e(t) = 3d_i - d_i \cos(2nt) - 2r_i \sin(nt) \tag{107}$$

To determine the minimum distance in the $\hat{\boldsymbol{e}}_1$ direction, the derivative is taken

$$\dot{X}_e(t) = 2d_i n \sin(2nt) - 2r_i n \cos(nt) \tag{108}$$

and set equal to zero, using the trigonometric identity $\sin(2nt) = 2\sin(nt)\cos(nt)$:

$$0 = 2\cos(nt)\big(2d_i \sin(nt) - r_i\big) = 2\cos(f)\big(2d_i \sin(f) - r_i\big) \tag{109}$$

For $-\pi \leq f \leq \pi$ and non-negative r_i and d_i, the roots of this equation are $\pm\frac{\pi}{2}$, and if $\frac{r_i}{2d_i} < 1$ then also $f = \arcsin\left(\frac{r_i}{3d_i}\right)$ and $f = \pi - \arcsin\left(\frac{r_i}{2d_i}\right)$. The second derivative of Eq. (107) shows that the latter two roots, if existing, always correspond to minima, while $f = -\frac{\pi}{2}$ always corresponds to a maximum. The root at $f = \frac{\pi}{2}$ only corresponds to a minimum if $\frac{r_i}{2d_i} \geq 1$, in which case the minimum is negative. If $0 < \frac{r_i}{2d_i} < 1$, the root at $f = \frac{\pi}{2}$ is neither a minimum nor a maximum (see Fig. 8), and if $r_i = 0$ it is a maximum. This results in the minimum distance

$$X_{e,\min}(r_i, d_i) = \begin{cases} 2d_i\left(1 - \left(\frac{r_i}{2d_i}\right)^2\right) & \text{at} \quad f = \arcsin\left(\frac{r_i}{2d_i}\right) \quad \text{if} \quad 0 \leq \frac{r_i}{2d_i} < 1 \\ 4d_i\left(1 - \frac{r_i}{2d_i}\right) & \text{at} \quad f = \frac{\pi}{2} \quad \text{if} \quad \frac{r_i}{2d_i} \geq 1 \end{cases} \tag{110}$$

Note that the first case occur at $f = \arcsin\left(\frac{r_i}{2d_i}\right)$ or $f = \pi - \arcsin(\frac{r_i}{2d_i})$. To avoid circumnavigation of the servicer around the target and for the minimum X_e distance to lie on the positive side, $\frac{r_i}{2d_i} < 1$. Thus, for a given $d_i = 10$ m, the required r_i to remain outside the wake is obtained by $r_{i,\text{req}} = \sqrt{2d_i(2d_i - X_{e,\min})}$. This yields $r_i = 14.142$ m for $X_{e,\min} = r_c = 10$ m. Finally, a rotation angle of $\alpha_i = 90$ deg is used to move the relative orbit outside of the wake. The corresponding inertial frame relative orbit and keep-out zone are shown in Fig. 13a.

Alternatively, a relative orbit with out-of plane motion may be chosen, as shown in Fig. 13b. In this case, the in-plane rotation α_i can remain zero, but an out-of-plane rotation $\beta_i = 90$ deg must be introduced to satisfy the keep-out constraint. Figure 14 shows the *YZ*-plane projection of the relative motion for the same relative orbits as in Fig. 13 to clearly show the satisfaction of the keep-out constraint.

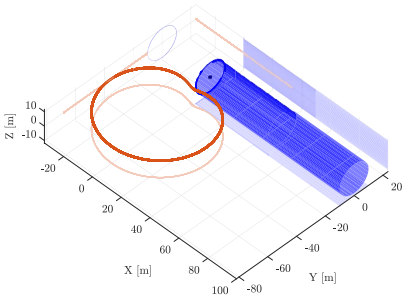

(a) Motion 1: $r_{i,0} = 14.142$ m, $\phi_{i,0} = 90$ deg, $d_i = 10$ m, $\alpha_i = 90$ deg, $B_i = 0$ m, $\beta_i = 0$ deg

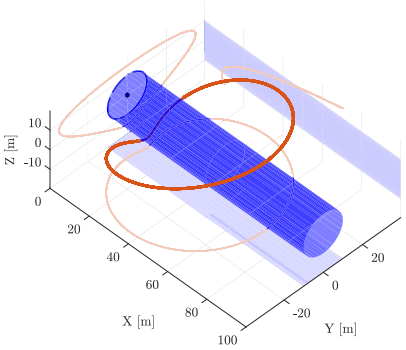

(b) Motion 2: $r_{i,0} = 15$ m, $\phi_{i,0} = 90$ deg, $d_i = 10$ m, $\alpha_i = 0$ deg, $B_i = 15$ m, $\beta_i = 90$ deg

Fig. 13 Relative motion in Inertial frame subject to cylindrical keep-out zone

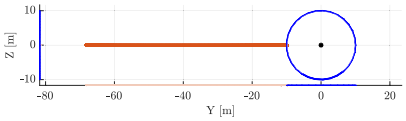

(a) Motion 1: $r_{i,0} = 14.142$ m, $\phi_{i,0} = 90$ deg, $d_i = 10$ m, $\alpha_i = 90$ deg, $B_i = 0$ m, $\beta_i = 0$ deg

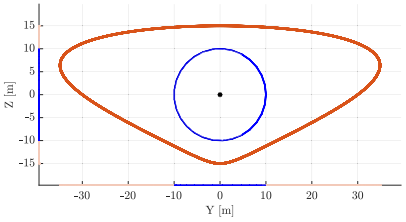

(b) Motion 2: $r_{i,0} = 15$ m, $\phi_{i,0} = 90$ deg, $d_i = 10$ m, $\alpha_i = 0$ deg, $B_i = 15$ m, $\beta_i = 90$ deg

Fig. 14 Relative motion in Inertial frame subject to cylindrical keep-out zone, *YZ*-plane projection

7 Conclusions

This paper investigates the relative motion of two spacecraft as seen from a frame that is centered at the chief spacecraft and with axes that are aligned with an inertial frame. Such an inertial frame description is beneficial compared to the conventional rotating Hill frame when the relative motion is subject to inertially fixed constraints. Examples for such missions include inertial targets for distributed space telescopes and coronagraphs, spacecraft formations and servicing operations with constraints imposed by the Sun (lighting conditions, eclipses, space plasma conditions, etc.), as well as rendezvous with a non-rotating target. The last example is relevant because the body frame of a non-rotating body remains aligned with the inertial frame, and body frames are frequently used for servicing and docking operations.

It is found that the inertial frame relative motion for a circular chief orbit is equivalent to the epitrochoid curve, in which a circle rolls without slip on a fixed circle, and the curve is generated by a point that is at a certain distance away from the center of the rolling circle. Thus, inertial frame relative orbit elements (IROEs) are defined that are based on the parameters of an epitrochoid curve and correspond to the invariants

of relative motion in the inertial frame. This allows for an intuitive description of the inertial frame relative motion. For elliptic chief orbits, the inertial frame relative orbits are stretched and distorted compared to the epitrochoid curve for circular chief orbits, but similar IROEs are defined as well. The variational equations of the IROEs are developed and applied to an asymptotically stabilizing continuous feedback control law. Finally, the IROE description is applied to an on-orbit servicing example, illustrating the intuitive relative orbit design process with inertial frame relative orbit elements.

Appendix 1 Cartesian Hill State to Linearized Relative Orbit Elements

The inverse mapping between the cartesian state in the Hill frame $\boldsymbol{s} = [x, y, z, \dot{x}, \dot{y}, \dot{z}]^T$ and the linearized relative orbit elements (LROEs) $\delta\boldsymbol{oe}_{CW} = [A_0, \alpha, x_{\text{off}}, y_{\text{off}}, B_0, \beta]^T$ used in Eq. (14) is obtained by solving Eqs. (14) and (17) for the LROEs and is equal to [26]

$$A_0 = \frac{\sqrt{9n^2x^2 + \dot{x}^2 + 12nx\dot{y} + 4\dot{y}^2}}{n} \tag{111}$$

$$\alpha = \arctan\left(\frac{-\dot{x}}{-3nx - 2\dot{y}}\right) - nt \tag{112}$$

$$x_{\text{off}} = 4x + 2\frac{\dot{y}}{n} \tag{113}$$

$$y_{\text{off}} = -2\frac{\dot{x}}{n} + y + (6nx + 3\dot{y})t \tag{114}$$

$$B_0 = \frac{\sqrt{n^2z^2 + \dot{z}^2}}{n} \tag{115}$$

$$\beta = \arctan\left(\frac{-\dot{z}}{zn}\right) - nt \tag{116}$$

Appendix 2 Inertial Frame Relative Orbit Elements to Linearized Relative Orbit Elements

The inverse mapping between the inertial frame relative orbit elements (IROEs) $\delta\boldsymbol{oe}_i = [r_i, \phi_i, d_i, \alpha_i, B_i, \beta_i]^T$ used in Eq. (37) and the linearized relative orbit elements (LROEs) $\delta\boldsymbol{oe}_{CW} = [A_0, \alpha, x_{\text{off}}, y_{\text{off}}, B_0, \beta]^T$ used in Eq. (14) is obtained by solving the relations in Eq. (37) for the LROEs. Four of those relations are trivially solved:

$$A_0 = 2d_i \tag{117}$$

$$\alpha = -\alpha_i \tag{118}$$

$$B_0 = B_i \tag{119}$$

$$\beta = -\beta \tag{120}$$

Using the relation for ϕ_i in Eq. (37)

$$\phi_i = \arctan\left(\frac{y_{\text{off}} - \frac{3}{2}ntx_{\text{off}}}{-x_{\text{off}}}\right) \tag{121}$$

and substituting into the relation for r_i in Eq. (37)

$$r_i = \frac{1}{2}\sqrt{\left(y_{\text{off}} - \frac{3}{2}ntx_{\text{off}}\right)^2 + x_{\text{off}}^2} \tag{122}$$

gives

$$\begin{aligned}(2r_i)^2 &= \left(y_{\text{off}} - \frac{3}{2}ntx_{\text{off}}\right)^2 + x_{\text{off}}^2 \\ (2r_i)^2 &= x_{\text{off}}^2 \tan^2\phi_i + x_{\text{off}}^2 = x_{\text{off}}^2(\tan^2\phi_i + 1) \\ (2r_i)^2 &= \left(\frac{x_{\text{off}}}{\cos\phi_i}\right)^2\end{aligned} \tag{123}$$

Solving for x_{off}, one obtains

$$x_{\text{off}} = \pm 2r_i \cos\phi_i \tag{124}$$

Looking at Eq. (121), one finds that if $x_{\text{off}} > 0$ then $\frac{\pi}{2} < \phi_i < \frac{3\pi}{2}$ and consequently $\cos\phi_i < 0$. Thus, because $r_i > 0$, the minus sign in the above equation applies, leading to

$$x_{\text{off}} = -2r_i \cos\phi_i \tag{125}$$

In a similar fashion, using Eqs. (122) and (125) give

$$y_{\text{off}} = 2r_i(\pm\sin\phi_i - \frac{3}{2}nt\cos\phi_i) \tag{126}$$

Looking at Eq. (121), one finds that if $y_{\text{off}} - \frac{3}{2}ntx_{\text{off}} > 0$ then $0 < \phi_i < \pi$ and consequently $\sin\phi_i > 0$. Thus, because $r_i > 0$, the plus sign in the above equation applies, leading to

$$y_{\text{off}} = 2r_i(\sin\phi_i - \frac{3}{2}nt\cos\phi_i) \tag{127}$$

This yields the mapping from IROEs to LROEs:

$$A_0 = 2d_i \tag{128}$$

$$\alpha = -\alpha_i \tag{129}$$

$$x_{\text{off}} = -2r_i\cos\phi_i \tag{130}$$

$$y_{\text{off}} = 2r_i\left(\sin\phi_i - \frac{3}{2}nt\cos\phi_i\right) \tag{131}$$

$$B_0 = B_i \tag{132}$$

$$\beta = -\beta_i \tag{133}$$

Appendix 3 Inertial Frame Relative Orbit Elements to Differential Orbit Elements

The inverse mapping between the inertial frame relative orbit elements (IROEs) $\delta\boldsymbol{\alpha e}_i = [r_i, \phi_i, d_i, \alpha_i, B_i, \beta_i]^T$ used in Eq. (37) and the differential orbit elements (DOEs) $\delta\boldsymbol{\alpha e} = [\delta a, \delta e, \delta i, \delta\Omega, \delta\omega, \delta M]^T$ used in Eq. (24) is obtained by solving the relations in Eq. (37) for the DOEs. Using a similar approach to the one in Appendix 2 and the relation $\eta = \sqrt{1-e^2}$ yields the mapping from IROEs to DOEs:

$$\delta a = -2r_i\cos\phi_i \tag{134}$$

$$\delta e = -2\frac{d_i}{a}\eta^2\cos\alpha_i \tag{135}$$

$$\delta i = \frac{B_i}{a}\sin\beta_i \tag{136}$$

$$\delta\Omega = -\frac{B_i}{a}\frac{\cos\beta_i}{\sin i} \tag{137}$$

$$\delta\omega = 2\frac{r_i}{a}\sin\phi_i - 2\frac{d_i}{ae}\sin\alpha_i + \frac{B_i}{a}\frac{\cos\beta_i}{\tan i} \tag{138}$$

$$\delta M = 2\frac{d_i}{ae}\eta^3\sin\alpha_i \tag{139}$$

Appendix 4 Cartesian Perifocal State to Inertial Frame Relative Orbit Elements

The inverse mapping between the cartesian state in the perifocal frame $\boldsymbol{s}_p = [X_p, Y_p, Z_p, \dot{X}_p, \dot{Y}_p, \dot{Z}_p]^T$ and the time-invariant inertial frame relative orbit elements (IROEs) $\delta\boldsymbol{\alpha e}_{i,0} = [r_{i,0}, \phi_{i,0}, d_i, \alpha_i, B_i, \beta_i]^T$ used in Eq. (63) is obtained by solving Eq. (63) and Eq. (66) for the time-invariant IROEs and is equal to

$$r_{i,0} = \frac{1}{2n}\sqrt{\begin{aligned}&\Big((X_p n - 2\dot{Y}_p)\sin(nt) - (Y_p n + 2\dot{X}_p)\cos(nt)\\&\quad - 3nt\big((\dot{X}_p - Y_p n)\sin(nt) - (X_p n + \dot{Y}_p)\cos(nt)\big)\Big)^2\\&+ \Big(2\big((\dot{X}_p - Y_p n)\sin(nt) - (X_p n + \dot{Y}_p)\cos(nt)\big)\Big)^2\end{aligned}} \tag{140}$$

$$\phi_{i,0} = \arctan\left(\frac{(X_p n - 2\dot{Y}_p)\sin(nt) - (Y_p n + 2\dot{X}_p)\cos(nt)}{2\big((\dot{X}_p - Y_p n)\sin(nt) - (X_p n + \dot{Y}_p)\cos(nt)\big)} - \frac{3}{2}nt\right) \tag{141}$$

$$d_i = \frac{1}{2n}\sqrt{\begin{aligned}&\Big((X_p n - \dot{Y}_p)\sin(nt) - (Y_p n + \dot{X}_p)\cos(nt)\Big)^2\\&+ \Big((2\dot{X}_p - Y_p n)\sin(nt) - (X_p n + 2\dot{Y}_p)\cos(nt)\Big)^2\end{aligned}} \tag{142}$$

$$\alpha_i = nt - \arctan\left(\frac{(X_p n - \dot{Y}_p)\sin(nt) - (Y_p n + \dot{X}_p)\cos(nt)}{(2\dot{X}_p - Y_p n)\sin(nt) - (X_p n + 2\dot{Y}_p)\cos(nt)}\right) \tag{143}$$

$$B_i = \frac{\sqrt{Z_p^2 n^2 + \dot{Z}_p^2}}{n} \tag{144}$$

$$\beta_i = nt - \arctan\left(\frac{-\dot{Z}_p}{Z_p n}\right) \tag{145}$$

Subsequently using Eqs. (61) and (62), the inverse mapping between the cartesian state in the perifocal frame $\boldsymbol{s}_p = [X_p, Y_p, Z_p, \dot{X}_p, \dot{Y}_p, \dot{Z}_p]^T$ and the general inertial frame relative orbit elements (IROEs) $\delta\boldsymbol{\alpha e}_i = [r_i, \phi_i, d_i, \alpha_i, B_i, \beta_i]^T$ used in Eq. (33) is obtained:

$$r_i = \frac{1}{2n}\sqrt{\begin{aligned}&\Big((X_p n - 2\dot{Y}_p)\sin(nt) - (Y_p n + 2\dot{X}_p)\cos(nt)\\&+ \Big(2\big((\dot{X}_p - Y_p n)\sin(nt) - (X_p n + \dot{Y}_p)\cos(nt)\big)\Big)^2\end{aligned}} \tag{146}$$

$$\phi_i = \arctan\left(\frac{(X_p n - 2\dot{Y}_p)\sin(nt) - (Y_p n + 2\dot{X}_p)\cos(nt)}{2\big((\dot{X}_p - Y_p n)\sin(nt) - (X_p n + \dot{Y}_p)\cos(nt)\big)}\right) \tag{147}$$

$$d_i = \frac{1}{2n}\sqrt{\begin{aligned}&\Big((X_p n - \dot{Y}_p)\sin(nt) - (Y_p n + \dot{X}_p)\cos(nt)\Big)^2 \\ &+ \Big((2\dot{X}_p - Y_p n)\sin(nt) - (X_p n + 2\dot{Y}_p)\cos(nt)\Big)^2\end{aligned}} \tag{148}$$

$$\alpha_i = nt - \arctan\left(\frac{(X_p n - \dot{Y}_p)\sin(nt) - (Y_p n + \dot{X}_p)\cos(nt)}{(2\dot{X}_p - Y_p n)\sin(nt) - (X_p n + 2\dot{Y}_p)\cos(nt)}\right) \tag{149}$$

$$B_i = \frac{\sqrt{Z_p^2 n^2 + \dot{Z}_p^2}}{n} \tag{150}$$

$$\beta_i = nt - \arctan\left(\frac{-\dot{Z}_p}{Z_p n}\right) \tag{151}$$

Acknowledgements Julian Hammerl gratefully acknowledges funding from the NASA FINESST fellowship (award number 80NSSC22K1849).

Author Contributions J.H. wrote the main manuscript text and prepared the figures, while H.S. provided guidance. All authors reviewed the manuscript.

Data Availability No datasets were generated or analysed during the current study.

Declarations

Conflict of interest On behalf of all authors, the corresponding author states that there is no conflict of interest.

References

1. Hill, G.W.: Researches in the lunar theory. Am. J. Math. **1**(1), 5–26 (1878). https://doi.org/10.2307/2369430
2. Clohessy, W.H., Wiltshire, R.S.: Terminal guidance system for satellite rendezvous. J. Aerosp. Sci. **27**(9), 653–658 (1960). https://doi.org/10.2514/8.8704

3. Koenig, A.W., D'Amico, S., Macintosh, B., Titus, C.J.: Optimal formation design of a miniaturized distributed occulter/telescope in earth orbit. In: 2015 AAS/AIAA Astrodynamics Specialist Conference, pp. 1–29 (2015)
4. Kolmas, J., Banazadeh, P., Koenig, A.W., Macintosh, B., D'Amico, S.: System design of a miniaturized distributed occulter/telescope for direct imaging of star vicinity. In: 2016 IEEE Aerospace Conference, pp. 1–11 (2016). https://doi.org/10.1109/AERO.2016.7500783
5. Koenig, A., D'Amico, S., Lightsey, E.G.: Formation flying orbit and control concept for the visors mission. In: AIAA Scitech 2021 Forum, pp. 1–22 (2021)
6. Cash, W., Oakley, P., Turnbull, M., Glassman, T., Lo, A., Polidan, R., Kilston, S., Noecker, C.: The new worlds observer: scientific and technical advantages of external occulters. In: Jr., J.M.O., Graauw, M.W.M., MacEwen, H.A. (eds.) Space Telescopes and Instrumentation 2008: Optical, Infra-Red, and Millimeter, vol. 7010, p. 70101. SPIE (2008). https://doi.org/10.1117/12.789717
7. Glassman, T., Lo, A.S., Arenberg, J., Cash, W., Noecker, C.: Starshade scaling relations. In: Shaklan, S.B. (ed.) Techniques and Instrumentation for Detection of Exoplanets IV, vol. 7440, p. 744013. SPIE (2009). https://doi.org/10.1117/12.825033
8. Aung, M., Ahmed, A., Wette, M., Scharf, D., Tien, J., Purcell, G., Regehr, M., Landin, B.: An overview of formation flying technology development for the terrestrial planet finder mission. In: 2004 IEEE Aerospace Conference Proceedings (IEEE Cat. No.04TH8720), vol. 4, pp. 2667–26794 (2004). https://doi.org/10.1109/AERO.2004.1368062
9. Quanz, S.P., Ottiger, M., Fontanet, E., Kammerer, J., Menti, F., Dannert, F., Gheorghe, A., Absil, O., Airapetian, V. S., Alei, E., Allart, R., Angerhausen, D., Blumenthal, S., Buchhave, L. A., Cabrera, J., Carrión-González, Ó., Chauvin, G., Danchi, W. C., Dandumont, C., Defrére, D., Dorn, C., Ehrenreich, D., Ertel, S., Fridlund, M., García Muñoz, A., Gascón, C., Girard, J.H., Glauser, A., Grenfell, J. L., Guidi, G., Hagelberg, J., Helled, R., Ireland, M.J., Janson, M., Kopparapu, R. K., Korth, J., Kozakis, T., Kraus, S., Léger, A., Leedjärv, L., Lichtenberg, T., Lillo-Box, J., Linz, H., Liseau, R., Loicq, J., Mahendra, V., Malbet, F., Mathew, J., Mennesson, B., Meyer, M.R., Mishra, L., Molaverdikhani, K., Noack, L., Oza, A. V., Pallé, E., Parviainen, H., Quirrenbach, A., Rauer, H., Ribas, I., Rice, M., Romagnolo, A., Rugheimer, S., Schwieterman, E.W., Serabyn, E., Sharma, S., Stassun, K. G., Szulágyi, J., Wang, H. S., Wunderlich, F., Wyatt, M. C., the LIFE Collaboration: Large interferometer for exoplanets (life)- i. improved exoplanet detection yield estimates for a large mid-infrared space-interferometer mission. Astron. Astrophys. **664**, 21 (2022) https://doi.org/10.1051/0004-6361/202140366
10. Scheeres, D., Vinh, N.: Dynamics and control of relative motion in an unstable orbit. In: Astrodynamics Specialist Conference, p. 4135 (2000)
11. Bucci, L., Colagrossi, A., Lavagna, M.: Rendezvous in lunar near rectilinear halo orbits. Adv Astronautics Sci. Technol. **1**, 39–43 (2018)
12. Franzini, G., Innocenti, M.: Relative motion dynamics in the restricted three-body problem. J. Spacecr. Rocket. **56**(5), 1322–1337 (2019). https://doi.org/10.2514/1.A34390
13. Khoury, F., Howell, K.C.: Orbital rendezvous and spacecraft loitering in the earth-moon system. In: AAS/AIAA Astrodynamics Specialist Conference, Lake Tahoe, California, USA, pp. 1–20 (2020)
14. Llorente, J.S., Agenjo, A., Carrascosa, C., de Negueruela, C., Mestreau-Garreau, A., Cropp, A., Santovincenzo, A.: PROBA-3: precise formation flying demonstration mission. Acta Astron. **82**(1), 38–46 (2013). https://doi.org/10.1016/j.actaastro.2012.05.029
15. Wang, J., Hastings, D.: Ionospheric plasma flow over large high-voltage space platforms. ii: the formation and structure of plasma wake. Phys. Fluids B Plasma Phys. **4**(6), 1615–1629 (1992)
16. Seubert, C.R., Stiles, L.A., Schaub, H.: Effective coulomb force modeling for spacecraft in earth orbit plasmas. Adv. Space Res. **54**(2), 209–220 (2014). https://doi.org/10.1016/j.asr.2014.04.005
17. Wilson, K., Schaub, H.: Impact of electrostatic perturbations on proximity operations in high earth orbits. J. Spacecr. Rocket. **58**(5), 1293–1302 (2021). https://doi.org/10.2514/1.A35039
18. Hastings, D.E.: A review of plasma interactions with spacecraft in low earth orbit. J. Geophys. Res. Space Phys. **100**(A8), 14457–14483 (1995). https://doi.org/10.1029/94JA03358
19. Ergun, R.E., Malaspina, D.M., Bale, S.D., McFadden, J.P., Larson, D.E., Mozer, F.S., Meyer-Vernet, N., Maksimovic, M., Kellogg, P.J., Wygant, J.R.: Spacecraft charging and ion wake formation in the near-sun environment. Phys. Plasmas **17**(7), 072903 (2010). https://doi.org/10.1063/1.3457484
20. Champion, K., Schaub, H.: Cislunar touchless potential sensing through barriers. In: Applied Space Environments Conference, Kauai, Hawaii, pp. 1–24 (2025)
21. Sullivan, J., Grimberg, S., D'Amico, S.: Comprehensive survey and assessment of spacecraft relative motion dynamics models. J. Guid. Control Dyn. **40**(8), 1837–1859 (2017). https://doi.org/10.2514/1.G002309

22. Alfriend, K., Vadali, S.R., Gurfil, P., How, J., Breger, L.: Spacecraft formation flying: dynamics, control and navigation, vol. 2. Butterworth-Heinemann, Burlington (2009)
23. Tschauner, J., Hempel, P.: Rendezvous zu einem in elliptischer bahn umlaufenden ziel. Astron. Acta **11**(2), 104–109 (1965)
24. Broucke, R.A.: Solution of the elliptic rendezvous problem with the time as independent variable. J. Guid. Control Dyn. **26**(4), 615–621 (2003). https://doi.org/10.2514/2.5089
25. Newman, B.A., Sinclair, A.J., Lovell, A., Perez, A.: Comparison of nonlinear analytical solutions for relative orbital motion. In: AIAA/AAS Astrodynamics Specialist Conference, pp. 1–29 (2014). https://doi.org/10.2514/6.2014-4163
26. Bennett, T., Schaub, H.: Continuous-time modeling and control using nonsingular linearized relative-orbit elements. J. Guid. Control Dyn. **39**(12), 2605–2614 (2016). https://doi.org/10.2514/1.G000366
27. Schaub, H., Vadali, S.R., Junkins, J.L., Alfriend, K.T.: Spacecraft formation flying control using mean orbit elements. J. Astron. Sci. **48**, 69–87 (2000). https://doi.org/10.1007/BF03546219
28. Schaub, H., Alfriend, K.T.: J_2 invariant relative orbits for spacecraft formations. Celest. Mech. Dyn. Astron. **79**, 77–95 (2001)
29. Schaub, H.: Relative orbit geometry through classical orbit element differences. J. Guid. Control Dyn. **27**(5), 839–848 (2004). https://doi.org/10.2514/1.12595
30. Koenig, A.W., Guffanti, T., D'Amico, S.: New state transition matrices for spacecraft relative motion in perturbed orbits. J. Guid. Control Dyn. **40**(7), 1749–1768 (2017). https://doi.org/10.2514/1.G002409
31. Gim, D.-W., Alfriend, K.T.: Satellite relative motion using differential equinoctial elements. Celest. Mech. Dyn. Astron. **92**, 295–336 (2005)
32. Alfriend, K.: Nonlinear considerations in satellite formation flying. In: AIAA/AAS Astrodynamics Specialist Conference and Exhibit, pp. 1–8 (2002). https://doi.org/10.2514/6.2002-4741
33. Montenbruck, O., Kirschner, M., D'Amico, S., Bettadpur, S.: E/I-vector separation for safe switching of the grace formation. Aerosp. Sci. Technol. **10**(7), 628–635 (2006). https://doi.org/10.1016/j.ast.2006.04.001
34. D'Amico, S., Montenbruck, O.: Proximity operations of formation-flying spacecraft using an eccentricity/inclination vector separation. J. Guid. Control. Dyn. **29**(3), 554–563 (2006). https://doi.org/10.2514/1.15114
35. Albert, S.W., Schaub, H.: Relative motion in the velocity frame for atmospheric entry trajectories. J. Spacecr. Rocket. **60**(5), 1614–1624 (2023). https://doi.org/10.2514/1.A35753
36. Roger, A.B., McInnes, C.R.: Safety constrained free-flyer path planning at the international space station. J. Guid. Control Dyn. **23**(6), 971–979 (2000). https://doi.org/10.2514/2.4656
37. Dong, H., Hu, Q., Akella, M.R.: Safety control for spacecraft autonomous rendezvous and docking under motion constraints. J. Guid. Control Dyn. **40**(7), 1680–1692 (2017). https://doi.org/10.2514/1.G002322
38. Naasz, B.: Safety ellipse motion with coarse sun angle optimization. In: 595 Flight Mechanics Symposium (2005)
39. Yao, Y., Xie, R., He, F.: Flyaround orbit design for autonomous rendezvous based on relative orbit elements. J. Guid. Control Dyn. **33**(5), 1687–1692 (2010). https://doi.org/10.2514/1.48494
40. Schaub, H., Junkins, J.L.: Analytical mechanics of space. Systems AIAA Education Series, 4th edn. Reston (2018). https://doi.org/10.2514/4.105210
41. Lovell, T.A., Tragesser, S.: Guidance for relative motion of low earth orbit spacecraft based on relative orbit elements. In: AIAA/AAS Astrodynamics Specialist Conference and Exhibit (2004). https://doi.org/10.2514/6.2004-4988